

## Article

# Proton-Exchange Membrane Fuel Cell Balance of Plant and Performance Simulation for Vehicle Applications

Tino Vidović, Ivan Tolj \*, Gojmir Radica  and Natalia Bodrožić ČokoFaculty of Electrical Engineering, Mechanical Engineering and Naval Architecture,  
University of Split, R. Boškovića 32, 21000 Split, Croatia

\* Correspondence: itolj@fesb.hr

**Abstract:** In this study, a newly developed zero-dimensional electrochemical model was used for modeling and controlling proton-exchange membrane fuel cell (PEMFC) performance. Calibration of the model was performed with measurements from the fuel cell stack. Subsequently, a compressor and a humidifier on the cathode side were sized and added to the existing model. The aim of this work was to model the PEMFC stack and balance of plant (BoP) components in detail to show the influence of operating parameters such as cathode pressure, stack temperature and cathode stoichiometric ratio on the performance and efficiency of the overall system compared to the original model using a newly developed real-time model. The model managed to predict the profile of essential parameters, such as temperature, pressure, power, voltage, etc. The most important conclusions from this particular case are: the cell power output is only slightly changed with the variations in stoichiometric ratio of the cathode side and adding an external compressor is valid only for high current applications, but in those cases, there is 10–22% power gain. Stack temperature is a very influential parameter. Optimal temperatures were determined through design of experiments (DoE) and for this case are in the 40–60 °C range, where for low current applications lower temperatures are better due lower activation loss (8% difference between 80 °C and 40 °C at 20 A current). For high current applications, due to lower ohmic losses, higher temperatures are desirable.

**Keywords:** proton-exchange membrane fuel cells; system modeling; balance of plant component sizing



**Citation:** Vidović, T.; Tolj, I.; Radica, G.; Bodrožić Čoko, N. Proton-Exchange Membrane Fuel Cell Balance of Plant and Performance Simulation for Vehicle Applications. *Energies* **2022**, *15*, 8110. <https://doi.org/10.3390/en15218110>

Academic Editor: Tek Tjing Lie

Received: 30 September 2022

Accepted: 26 October 2022

Published: 31 October 2022

**Publisher's Note:** MDPI stays neutral with regard to jurisdictional claims in published maps and institutional affiliations.



**Copyright:** © 2022 by the authors. Licensee MDPI, Basel, Switzerland. This article is an open access article distributed under the terms and conditions of the Creative Commons Attribution (CC BY) license (<https://creativecommons.org/licenses/by/4.0/>).

## 1. Introduction

One of the most important topics being studied today is climate change and its effects [1,2]. World energy consumption increased by 2.9% in 2019. That is almost a 100% increase in comparison to the constant average of 1.5% per year over the last decade. Carbon emissions from energy production also increased by 2% compared to the year before, which is alarming growth, with total emissions approaching 0.6 GT [3]. Unfortunately, fossil fuels continue to be the largest contributor to global energy demand. This creates problems as most fossil reserves are rapidly depleting and their prices are constantly fluctuating and volatile [4]. The research community has explored various ways to address this problem, such as improving the efficiency of fuel usage [5] and/or using various renewable energy sources. Additionally, many governments around the world have recognized the seriousness of finding a permanent solution for climate change [6]. This has led to the signing of numerous climate agreements between these countries to address this problem [7]. In particular, the Paris Agreement [8] and the Kyoto Protocol [9] are most influential. As a result, renewable sources of energy are considered as the only and inevitable substitute for fossil fuels. However, the irregularity of renewable energy sources is another demanding issue that prevents its full commercialization. One of the sources which does not produce any emissions and is highly energy dense is hydrogen. Recently, rapid progress in the production of green hydrogen (from various renewable energy sources) has been made. Hydrogen as a fuel can be combusted (in engines) or

electrochemically reacted (in fuel cells). As combustible fuel it can be directly injected into the internal combustion engine and leads to advantages, such as high volumetric efficiency, but also to potential backfire [10] and increased formation of NO<sub>x</sub> due to pre-ignition of the hydrogen–air mixture at high loads [11]. Those are several challenges that still need to be fully addressed.

As electrochemical fuel, hydrogen can be used in fuel cells. Fuel cells are electrochemical devices used for direct conversion of chemical energy (from various fuels) to electricity with high efficiency [12]. This is a significant advantage over any engine, since the losses during combustion and conversion in mechanical power systems are not present [13]. In addition to the higher efficiency, fuel cells are capable of providing completely emission-free power generation [14,15]. Hydrogen-powered fuel cell systems are becoming the energy system for future automotive [16,17] and heavy-duty transport [18], trains [19], buses [20], ships [21] and even planes [22]. However, the unsatisfactory lifespan of fuel cells is a great restriction for their full commercialization, so different health management strategies are still being developed [23]. The typical fuel cell system shown in Figure 1 [24] consists of the stack and the associated balance of plant (BoP) components that include a H<sub>2</sub> tank, heat exchanger, cooling system, air compressor, humidifier, power converters, etc. In a hybrid fuel cell system, other energy sources such as batteries and supercapacitors can also be integrated to further increase system efficiency and stability [25]. Crespi et al. [26] proved that, with addition of air expander, the additional energy recovery from the cathode exhaust can be made on MW-scale power plant. In addition, vehicles powered with are also compatible with the new emerging sector of coupled energy systems, where excess peaks in electricity generation from renewable sources, e.g. from wind turbines and photovoltaic cells, can be used to generate hydrogen through electrolysis [27].

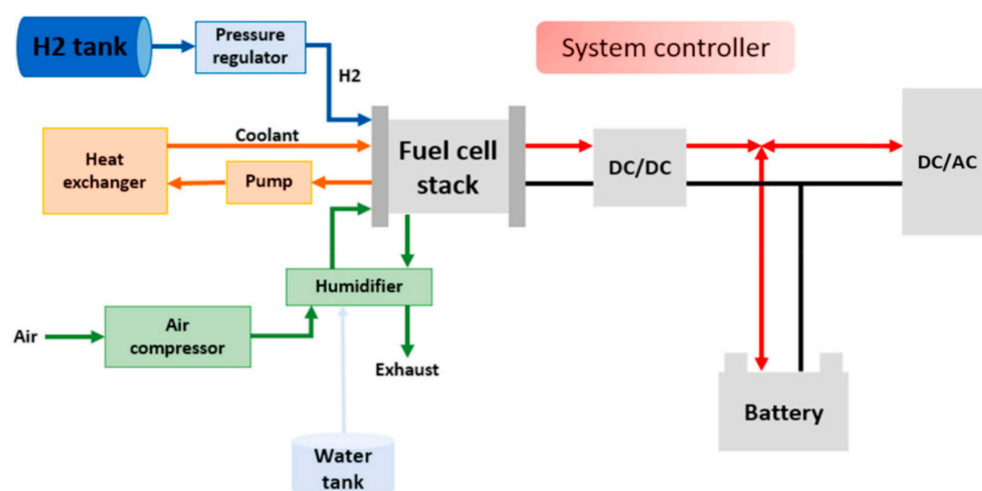


**Figure 1.** Schematic of a typical hybrid fuel cell system and balance of plants.

From the previous description, it can be concluded that the efficiency of the overall system depends not only on the fuel cell stack but also on auxiliary components. In this article, the fuel cell stack model is described in detail and calibrated with measurements. The novelty of this particular model is that, unlike the most commonly used fast electrochemical models with reduced dimensionality, it does not approximate the Butler–Volmer equation (BV) equation with the Tafel equation but uses the sinus hyperbolicus to reduce the BV equation. As a result, this model remains computationally fast and can be used in real time with good extrapolation capabilities for control strategies. Subsequently, a compressor and a humidifier on the cathode side were sized and added to the existing model. The aim of this work was to model the fuel cell stack and BoP components in detail with a real-time model and then a design of experiments was made to show the influence of operating parameters such as cathode pressure, stack temperature and cathode stoichiometric ratio on the performance and efficiency of the overall system compared to the original model.

## 2. Methodology

This chapter is divided into two subchapters: experimental setup and system modeling. In the first subchapter, one of the fuel cell stacks in our laboratory at the Faculty of Electrical Engineering, Mechanical Engineering and Naval Architecture in Split is presented. In addition to the stack, the boundary conditions and measurements are also listed. In the second subchapter, a detailed model of the fuel cell stack, the compressor and the humidifier components are explained.

### 2.1. Experimental Setup

Calibration of original model was performed with measurements from Nexa 1200 fuel cell stack. It is an air-cooled PEM stack with 36 fuel cells which, with an output voltage between 16 and 40 V and a maximum output current of 60 A at 5–25 °C, delivers a power output of 1200 W. The unit can be supplied with hydrogen (max inlet pressure 15 bar) by means of the lab supply with a downstream pressure reducer, an electrolyzer or metal hydride canisters. A fan provides the necessary reaction and cooling air through the housing to the stack. The housing not only holds the components but also functions to guide the air.

Before presenting the actual measurement results, it must be emphasized that this device has experienced performance degradation through use such that both the polarization curve and the nominal power deviate significantly from those stated in the specifications. Table 1 shows the measurement results from various operating points and Figure 2 shows the polarization curve of the stack. In addition to current and voltage, ambient air temperature, relative humidity, stack temperature and hydrogen consumption were also measured. Stoichiometric cathode ratio was set to 2 and cathode pressure was ambiental.

**Table 1.** Measurements taken from Nexa 1200 fuel cell stack at various load points.

Power [W]	100	200	300	400	500	600	687
Current [A]	4.07	8.8	13.63	18.8	24.97	32.8	41.3
Voltage [V]	24.55	22.98	22.09	21.24	20.04	18.3	16.7
Ambient air temperature [°C]	25	25	25	25	25	25	25
Relative humidity [-]	0.3	0.3	0.3	0.3	0.3	0.3	0.3
Stack temperature [°C]	38.3	40.2	41.8	42.2	43.5	44.4	45.6
Hydrogen consumption [L/min]	1.82	2.94	4.23	5.65	7.2	9.3	11.6

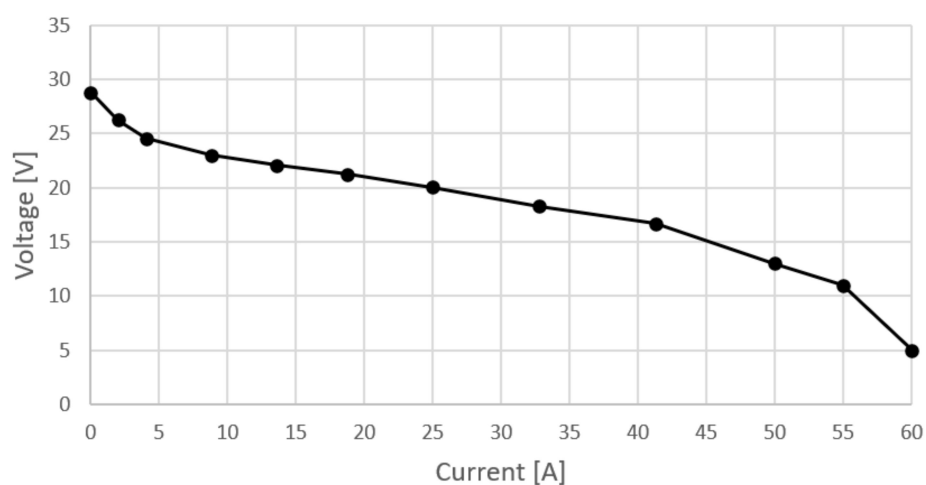


**Figure 2.** Polarization curve measured on Nexa 1200.

## 2.2. System Modeling

This subsection focuses on a detailed description of the model developed with AVL Cruise M software and used to calculate and calibrate the operating parameters of the entire system. The major system components discussed below are: fuel cell model, compressor model and humidifier model.

### 2.2.1. Fuel Cell Model

This model is based on research done by A. Kravos et al. [28]. It consists of a 0-dimensional, thermodynamically consistent electrochemical model for controlling PEMFC performance and is then extended so it accounts the transport of gaseous species across the channels and through the gas diffusion layer (GDL), which results in a quasi 1D electrochemical model.

In electrochemistry, the Butler–Volmer equation describes how the electrical current through an electrode depends on the voltage difference and for fuel cell, and it can be defined through following equation:

$$j_c = e^{-\frac{(A_0 + \alpha_c \Delta g_c^0 + \alpha_c \Delta s_c(T - T^0))}{k_B T}} \cdot e^{-\alpha_c \cdot \ln\left(\frac{k_{RDC}^*}{k_{OXC}^*}\right)} \cdot \left(\tilde{C}_{O_2}\right)^{(1 - \alpha_c)} \cdot \left(\tilde{C}_{H_2O}\right)^{2\alpha_c} k_{RDC}^* \left( e^{-\frac{\alpha_c e_0 Z_c \eta_c}{k_B T}} - e^{\frac{(1 - \alpha_c) e_0 Z_c \eta_c}{k_B T}} \right) \quad (1)$$

where  $j_c$  is cathodic net reaction rate,  $\tilde{C}_{O_2}$  and  $\tilde{C}_{H_2O}$  are the normalized concentrations of oxygen and water,  $k_{RDC}^*$  and  $k_{OXC}^*$  are reaction rate constants,  $k_B$  is the Boltzmann constant,  $T$  is the temperature,  $e_0$  is the elementary charge,  $\Delta g_c$  is the cathode side difference in specific Gibbs free energy between reactants and products,  $Z_c$  is the number of electrons transferred in the electrochemical reaction on the anode and cathode side,  $\alpha_c$  is the charge transfer coefficients on the cathode side,  $A_0$  represents energy needed to get to transition state, represents reaction kinetics overvoltage on the cathode. However, the development of a reduced dimensionality performance model revolving around the Butler–Volmer equation proves troublesome because of the difficulty in finding its inverse function. This is of utmost importance to facilitate the parameterization. Therefore, in previous works, researchers have mainly used two forms of a simplified version of the Butler–Volmer equation. The first forms are electrochemical models based on the Tafel equation, which is a reasonable approximation for operating points with high current densities but has a significant drawback in the low current density region, where the approximation error increases exponentially as the current density approaches zero. The second forms are electrochemical models based on the Tafel equation extended by various corrections for the low current density region. Proposed substitution successfully reduces the total error in the low current density region, but leads to incorrectly positioned individual terms in the equation for activation losses which can directly influence the calibration procedure and model performance.

Kravos et al. made the assumption that charge transfer coefficient  $\alpha_c$  (Equation (1)) is equal to 0.5, so simplification can be made through use of sinus hyperbolicus. This results in equation which is equivalent to Butler–Volmer equation and is accurate over all current densities. Therefore, the derivation stays thermodynamically consistent, but it loses a bit of generality. If the new equation is multiplied with factor  $ZF$ , where  $Z$  is number of electrons transferred in the electrochemical reaction and  $F$  is Faraday constant, we get net current on the cathode side:

$$I_c = I_0^c \cdot e^{-\frac{E_c^c}{k_B T}} \left(\tilde{C}_{O_2}\right)^{0.5} \left(\tilde{C}_{H_2O}\right) 2 \sinh\left(-\frac{e_0 Z_c \eta_c}{k_B T}\right) \quad (2)$$

$$I_0^c = ZF e^{-\frac{\alpha_c \Delta s_c(T - T^0)}{k_B T}} e^{-\alpha_c \cdot \ln\left(\frac{k_{RDC}^*}{k_{OXC}^*}\right)} k_{RDC}^* \quad (3)$$

From Equation (2), expression for reaction kinetics overpotential  $\eta_c$  can be made. All equations above are defined for cathode side but also can be derived for anode side. With that, the model is suitable to operate in fuel cell and in electrolyzer mode. The model considers both the anode and the cathode reaction, the latter of which is usually predominant in PEM fuel cells. The activation loss usually governs the voltage drop in the low current zone, i.e., the left side of the polarization curve.

The cell voltage  $U_{cell}$  is defined as:

$$U_{cell} = U_{th} - \eta_c - \eta_a - U_R \quad (4)$$

where  $U_{th}$  is the thermodynamic potential and  $U_R$  is voltage ohmic loss.

$U_{th}$  defines the voltage at open circuit conditions and is calculated from the ideal cell voltage  $\Delta E^0(T)$  and the Nernst voltage.

$$U_{th} = \Delta E^0(T) - \frac{R \cdot T}{2 \cdot F} \cdot \ln \left( \frac{C_{H_2O}}{C_{H_2} \cdot C_{O_2}^{0.5}} \right) \quad (5)$$

Ohmic losses are determined by proton transport across the membrane so they mainly affect ionic conductivity  $\sigma$ , which is determined from the property database. Assuming constant properties, the ohmic loss increases linearly with current density. It thus defines the slope of the polarization curve at medium current.

The transport loss describes the effects of diffusion of the species across the channel through the GDL into the catalyst layer. The process is described in a quasi-1D manner by Fick's law of diffusion. The process defines the limiting current densities, i.e., the current density at which the reactant concentration at the catalyst layer would decrease. In PEM fuel cells, the transport loss is usually more pronounced on the cathode side. The transport loss determines the polarization curve at high current densities and the limiting current. The concept behind the transport model is that concentration of reactants on the catalyst layer ( $C_{r_{CL}}$ ) can be calculated multiplying with the concentration of reactants in channel  $C_{r_{chan}}$  and ratio between limiting current ( $I_L$ ) and current density ( $I$ ) as following:

$$C_{r_{CL}} = C_{r_{chan}} \left( 1 - \frac{I}{I_L} \right) \quad (6)$$

$$I_L = ZFSD_{rr} \frac{C_{r_{chan}}}{\delta_{GDL}} \quad (7)$$

where  $D_{rr}$  is diffusion coefficient and  $\delta_{GDL}$  is GDL width. This electrochemical model offers 5 calibration coefficients, each correlating to one loss mechanism. The loss mechanisms (activation and transport loss) are usually more pronounced on the cathode side, so the parameters related to the anode can usually be omitted. Membrane material properties, such as density, specific heat capacity, thermal and ionic conductivity, water diffusion and electro-osmotic drag coefficients, are taken from [29].

### 2.2.2. Compressor

The air supply system is critical to the stable and efficient operation of a fuel cell system. First, it affects the humidity level (and humidity removal) of the stack. On the other hand, the oxygen content of the air affects the stack voltage and thus the efficiency of the stack. The air compressor can supply air to the stack at different air mass flow rates and air pressure levels. These operating parameters and the corresponding power consumption of the compressor influence the efficiency of the stack and the system. At higher pressures (above 150 kPa), the electric motor can consume a considerable amount of the total fuel

cell power output, as is clear in the Results Section. Assuming adiabatic compression, compressor power can be calculated as follows:

$$P_c = \dot{m} \cdot \frac{1}{\eta_{s,C}} \cdot c_p \cdot T_1 \cdot \left[ \left( \frac{p_{02}}{p_{01}} \right)^{\frac{\kappa-1}{\kappa}} - 1 \right] \quad (8)$$

where  $\dot{m}$  is mass flow through compressor,  $\eta_{s,C}$  compressor efficiency,  $c_p$  specific heat at constant pressure,  $T_1$  inlet temperature,  $p_{02}$  and  $p_{01}$  are inlet and outlet pressures and  $\kappa$  is ratio of the heat capacities. Pressure ratio and efficiency are function of corrected mass flow  $\dot{m}_{cor}$  and corrected rotational speed  $n_{cor}$  and are directly interpolated from compressor map which can be seen on Figure 3. Compressor map sizing is described in Section 3.2. Corrected mass flow and rotational speed can be calculated from the following equations and are used to take into account the influence of ambient conditions.

$$\dot{m}_{cor} = \frac{\dot{m} \cdot \sqrt{T_{01}}}{p_{01}} \quad (9)$$

$$n_{cor} = \frac{n}{\sqrt{T_{01}}} \quad (10)$$

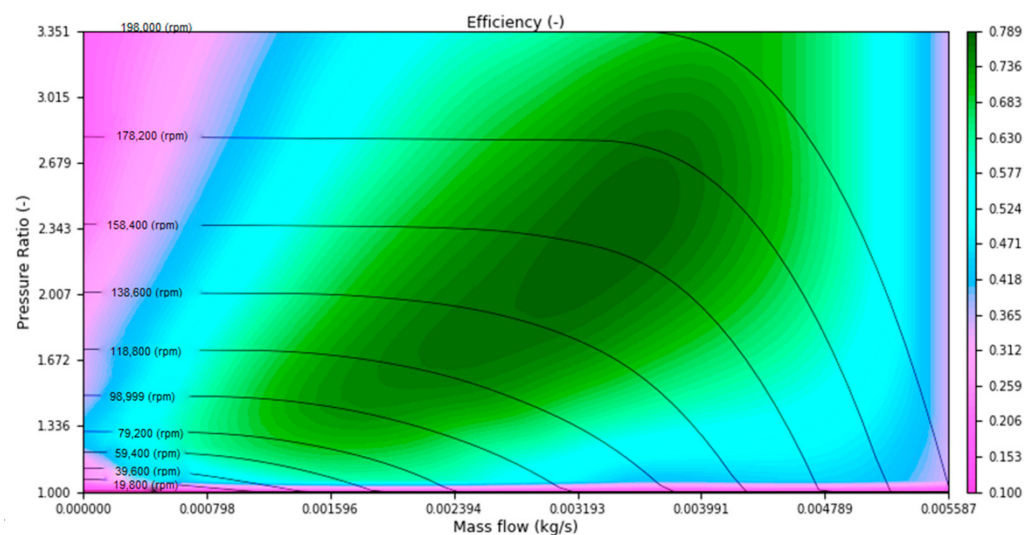


Figure 3. Compressor map [30].

### 2.2.3. Humidifier

The PEMFC is highly dependent on proper water management to achieve high efficiency [31]. Inadequate control of water accumulating at the cathode can cause excess water to accumulate at the cathode by flooding and block the gas pores used for oxygen transport, creating another barrier to transport across the reactive site. Flooding also results in excess water in the membrane–electrode assembly, reducing the catalytic area required for electrochemical reactions. Even simple fuel cell systems require auxiliary systems to wet the anode and dispose of the water from the cathode. In PEM fuel cell stacks, the goal of a humidifier is to control the relative humidity of the reactants so that the fuel cell membrane humidity remains close to 100% without flooding it. Other researchers have proposed various humidification mechanisms for PEM fuel cells. The most common are nozzle spray, gas bubbles, the “enthalpy wheel” [32] and membrane humidification. The membrane humidification model is explained below.

To derive the governing thermodynamic equations, the controls are defined, and for the membrane humidifier design, two control volumes (dry and humid) are defined as shown in Figure 4 [33]. The gas inlet mass flow rate, pressure, temperature, and relative humidity are inputs for both control volumes. The dry gas and the exhaust humid gas can

flow in parallel or counter flow pattern. Figure 4 shows that the dry gas and the exhaust gas flow in the counter flow arrangement. For both control volumes conservation of mass and energy equations are derived. Conservation of mass equation shows that change of mass of control volume is equal to difference between inlet and outlet flows with addition (for dry control volume) or subtraction (for humid control volume) of water vapor mass through membrane. The transferred vapor mass is determined by the membrane diffusion coefficient and the relative humidity gradient across the membrane and can be written as:

$$\frac{dm_v}{dt} = D_w \frac{C_2 - C_1}{t_m} M_v A \quad (11)$$

where  $M_v$  is the vapor molar mass,  $C_1$  and  $C_2$  represent water concentrations in control volumes,  $D_w$  diffusion coefficient,  $t_m$  membrane thickness and  $A$  is humidifier membrane area.

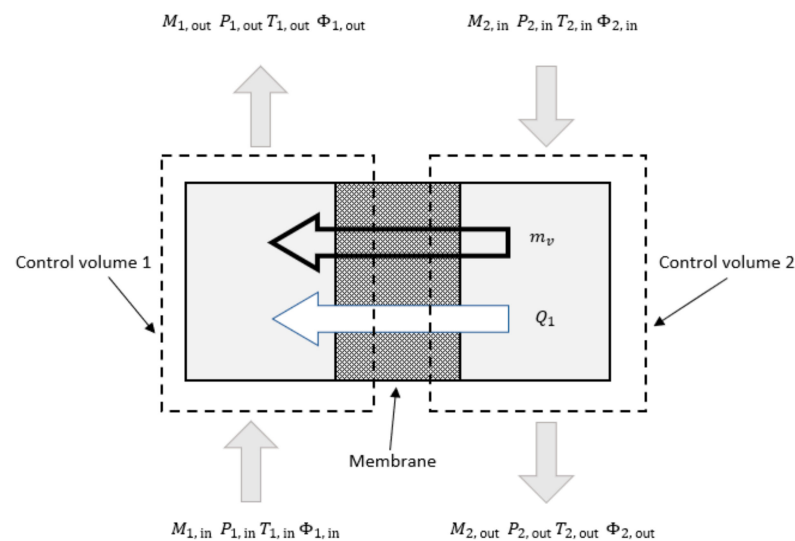


**Figure 4.** Control volumes of one humidifier unit.

Conservation of energy equation shows that change of control volume internal energy is equal to sum of enthalpy vapor mass, inlet and outlet flow and heat transfer rate between volumes. The heat transfer rate between the two control volumes is:

$$\frac{dQ_1}{dt} = UA\Delta T_{2/1} \quad (12)$$

where  $\Delta T_{2/1}$  is the log mean temperature difference between the two control volumes, and  $U$  is the overall heat transfer coefficient, defined as:

$$U = \frac{kN_{uD}}{2D_h} \quad (13)$$

where  $k$  is the membrane thermal conductivity,  $N_{uD}$  is the Nusselt number, and  $D_h$  is the channel hydraulic diameter.

### 3. Simulation Results

This chapter presents the calibration of the base model, the sizing of the newly added compressor and humidifier and the DoE process to determine the individual effects of various factors that influence the output results. After that, comparison of the efficiency and performance of the original and the improved model at different stoichiometric ratios is presented. Finally, the model with the best power output was selected and the effect of temperature on the operating parameters was further investigated. As mentioned before, the original stack is air-cooled. Since water and heat management are not in the scope of

this article, cooling is not directly defined, but the assumption is made that the temperature of the stack is constant without defining how this temperature is maintained.

### 3.1. Base Model Calibration

As stated in Section 2, the electrochemical fuel cell model offers five calibration parameters, each correlating to one loss mechanism. The voltage losses are usually more pronounced on the cathode side, so calibration parameters related to the anode side were not taken into account. After testing the model in a real-time environment, the cathode transport loss calibration parameter was left untouched, but ohmic and activation losses had to be raised. Ohmic losses mainly come from resistance of the ion flow in the electrolyte and electron flow resistance through the electrode. Membrane performance of the measured stack is not at its nominal state due to degradation, so its ionic conductivity is greatly reduced resulting in higher ohmic resistance. The ohmic loss calibration parameter had to be 50% larger than the default one. The cathode activation loss calibration parameter is set to be 10 times higher than the default one. Again, degradation is the main reason why these losses are so big. In Figure 5, the comparison between the simulated and measured polarization curve is presented. It can be clearly seen that the model sufficiently reflects experimental voltage vs. current profiles and establishes its very good extrapolation capabilities even outside the calibrated space of the parameters, demonstrating its robustness in a real-time environment.

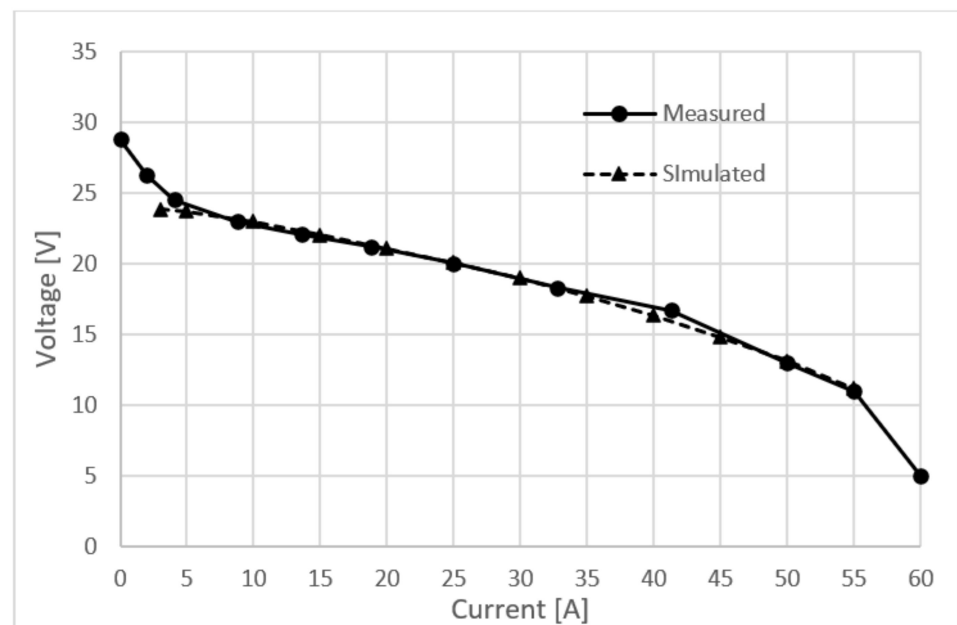


**Figure 5.** Measured and simulated polarization curve.

### 3.2. Compressor Sizing

To select the compressor map, the first step was to determine the required mass flow rate and the desired pressure ratio for various operating points. The operating points were determined with demanded current. To maintain stack stability, the mass flow of reactants at the fuel cell inlet must be equal or greater than the rate at which these reactants are depleted. The rates of hydrogen and oxygen consumption and water production are determined by Faraday's law; therefore, the mass flow rate can be calculated by the following equation:

$$\dot{m} = S_{O_2} * I * n_{\text{cells}} * \frac{M}{4 * c_{O_2} * F} \quad (14)$$

where  $S_{O_2}$  is the cathode stoichiometric ratio,  $I$  is the current,  $n_{\text{cells}}$  is the number of cells in stack,  $M$  is the air molar mass and  $c_{O_2}$  is the concentration of oxygen in air. It can be seen

that consumption of reactants in a fuel cell is proportional to the current and number of cells. The stoichiometric ratio is defined as a ratio between the real flow of reactant at the inlet and its theoretical consumption.

After that, the pressure ratio is calculated from the estimated heat exchanger and the humidifier pressure drops, and the demanded pressure and pipe pressure drop.

$$p_{\text{ratio}} = p_{\text{demand}} + dp_{\text{HEX}} + dp_{\text{humidifier}} + \frac{(I * dp_{\text{max}} / I_{\text{max}})}{p_{\text{ambient}}} \quad (15)$$

where  $p_{\text{demand}}$  is the pressure ratio demanded by the controller,  $dp_{\text{HEX}}$  is heat exchanger pressure ratio estimation,  $dp_{\text{humidifier}}$  is humidifier pressure ratio estimation,  $dp_{\text{max}}$  is maximal pipe pressure ratio estimation. Parameter  $p_{\text{demand}}$  is defined as a function of current and can be seen in Figure 6 and was selected based on recommendations from the literature. From the last two equations it can be seen that pressure ratio and mass flow are dependent on the fuel cell current.

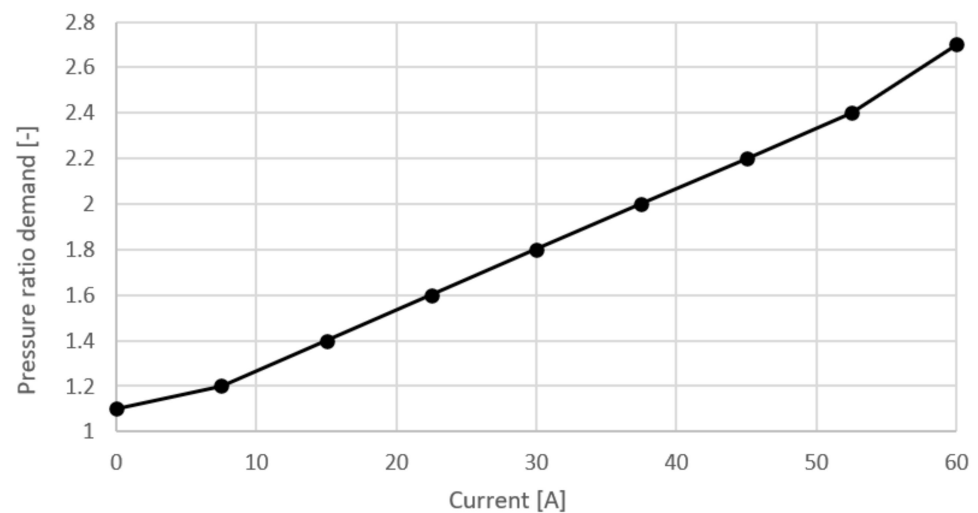


**Figure 6.** Pressure ratio demand.

Operational points were selected at zero (3 A) and max (60 A) load and two points at 20 and 40 A. All mass flows were calculated with the stoichiometric ratio equal to 2. In addition to the desired pressure ratio and mass flow rate, Table 2 also lists the temperature after compression, the heat flux required to bring the stack temperature to 60 °C, and the amount of steam required to saturate the fuel cell membrane. A compressor map is then selected from the catalog to match the calculated operating points. The selected map can be seen in Figure 3.

**Table 2.** Compressor and humidifier sizing parameters at various loads.

	Zero Load (3 A)	Operating Point 1 (20 A)	Operating Point 1 (40 A)	Max Load (60 A)
Heat exchanger heat rejection [W]	−1.7528	10.32	68.506	172.03
Temperature after compressor [°C]	37.451	79.915	126.1	170.66
Inlet mass flow [g/s]	0.0771919	0.514613	1.02923	1.54384
Pressure ratio [-]	1.1421103	1.5474018	2.0948037	2.7422055
Humidifier water vapor mass flow [g/s]	0.00326505	0.021767	0.043534	0.065301

### 3.3. Simulation Results for Various Stoichiometric Ratios

In [34] it was shown that lowering the cathode stoichiometry ratio so that condensation of water is happening in the cell can improve the ionic conductivity of the membrane. For this reason, too much cathode ventilation is undesirable, as is too little. A high gas flow through the cathode leads to a drying out of the membrane and thus to a cell efficiency reduction. Another criterion for optimizing cathode stoichiometry is economic. The demand for higher flow through the fuel cell cathode is directly associated with an increase in the total energy consumption and a reduction in oxygen utilization in the case of pure oxygen systems, thus contributing to a reduction in the system's overall efficiency. Figures 7 and 8 show how variation in stoichiometric ratio ( $S$ ) affects cell voltage, power, system efficiency and compressor power when a new compressor and humidifier are added, in comparison with the base model.

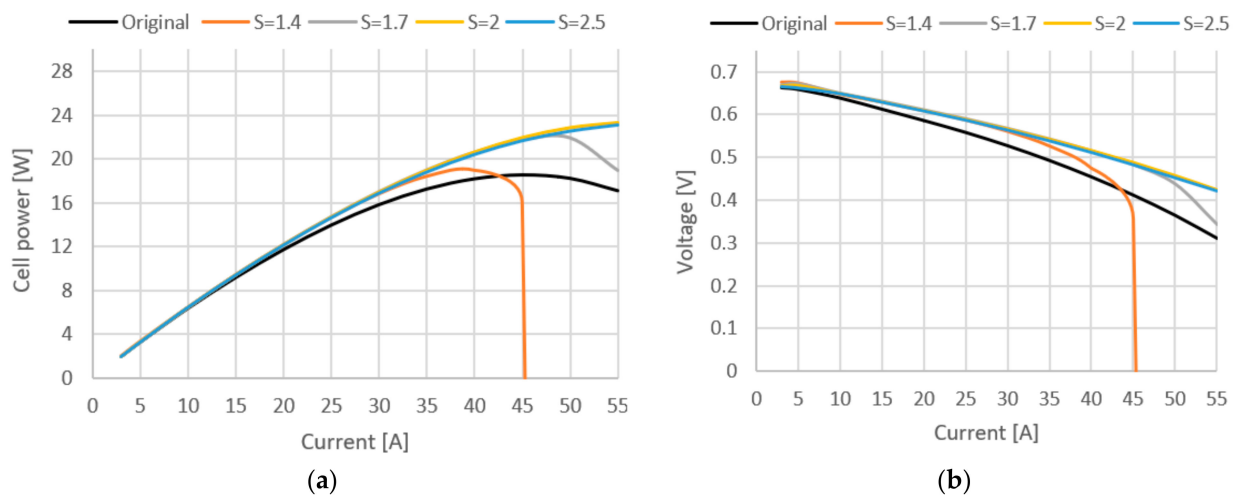


**Figure 7.** (a) Cell power curve at different stoichiometric ratios. (b) Cell voltage curve at different stoichiometric ratios.

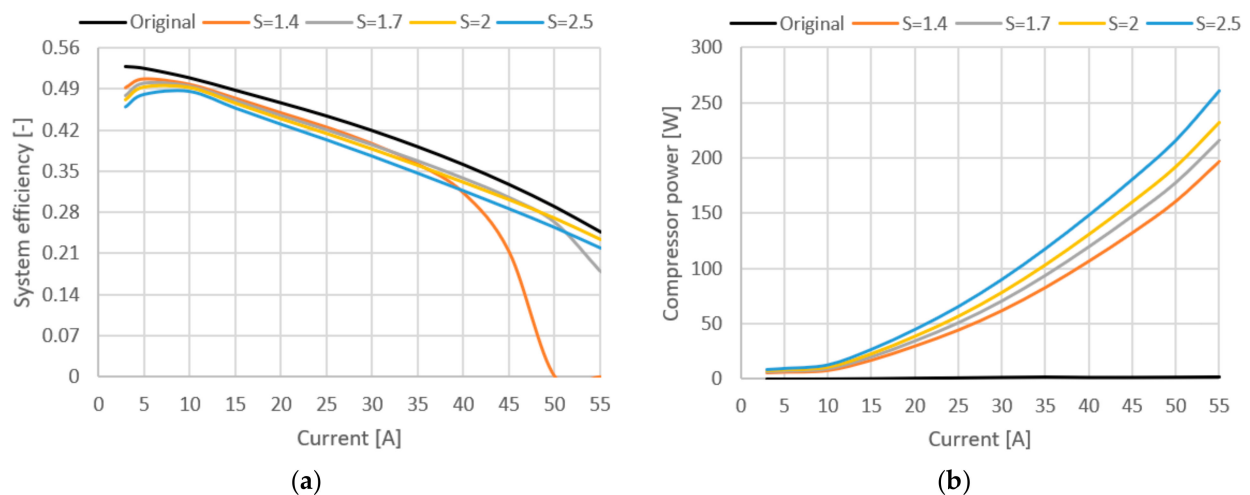


**Figure 8.** (a) System efficiency (stack and compressor). (b) Power loss due to compressor use.

In Figure 7, it can be seen how the stoichiometric ratio affects cell power and voltage. Adding compressor increased the cathode pressure, which had a positive effect on performance. This is because higher cell pressures increase the oxygen partial pressure in the channels, which in turn increases the open circuit voltage and reduces the overpotential of cathode activation. Furthermore, higher cell pressures increase water activity and content

in the membrane, which reduces the ohmic overpotential. As a result, both the cell voltage and the fuel cell power are increased by up to 22% at maximum load, and it can be seen that use of compressor does not yield any great benefits on lower current densities, but it takes toll on total system efficiency. Therefore, depending on the operating conditions of the fuel cell stack, the original model might be a better solution due to less fuel consumption and simpler design. The stoichiometric ratio has negligible effects in every case except when  $S = 1.4$ , at which not enough oxygen is provided to cell.

In Figure 8, it can be seen how the addition of the compressor affects the efficiency of the entire system. The biggest efficiency has the original stack where no compressor was used at all. The efficiency difference between the original and compressed model at the stoichiometric ratio of 2 is around 3%. Increasing the stoichiometric ratio increases the share of power losses for compressor operation, which can be seen in Figure 8b.

### 3.4. Simulation Results for Various Stack Temperatures

The effects of operating temperature on fuel cell performance are not easily predicted. An increase in temperature leads to a theoretical potential loss, but on the other hand, higher temperatures also bring many positive effects such as higher exchange current densities, better ionic conductivity and improved mass transfer properties. In addition, the gases can contain larger amounts of water vapor at higher temperatures, reducing the risk of flooding. Fuel cell performance generally improves with higher temperatures, but only up to a certain temperature, which can vary from cell to cell depending on design and operating conditions. Figure 9a,b show how variation of stack temperature affects cell voltage, power, system efficiency and fuel cell membrane water mass.

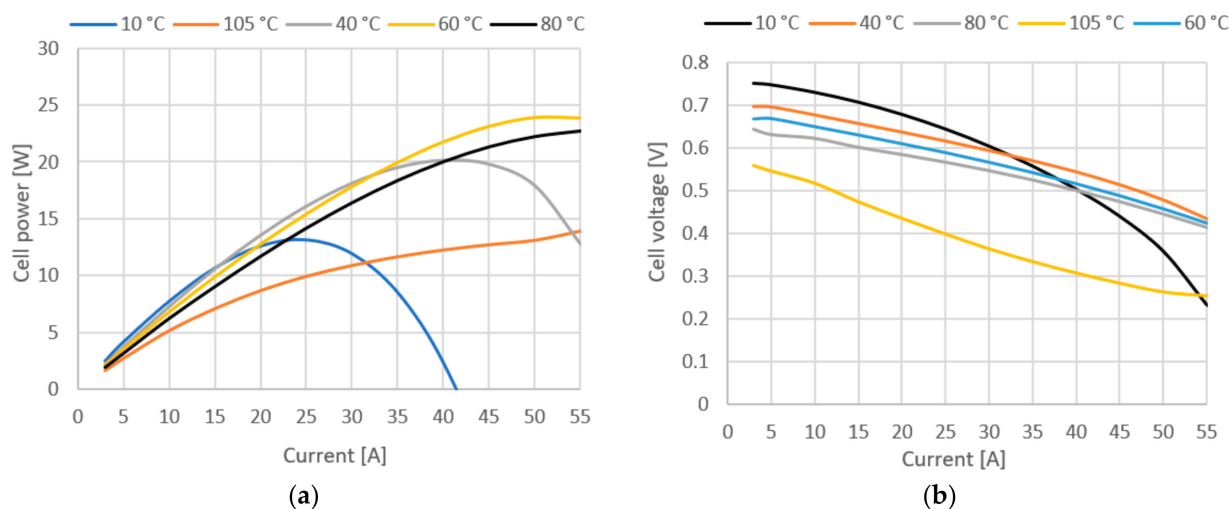


**Figure 9.** (a) Cell power at various stack temperatures. (b) Cell voltage at various stack temperatures.

Figure 9 shows cell power and voltage at various temperatures. Looking at voltage losses from Equation (4), they are strongly affected by temperature changes. Activation losses are lower at lower temperatures, resulting in higher open circuit voltages compared to high temperatures. On the other hand, the ohmic losses increase sharply with decreasing temperature, which is best seen when the fuel cell is operated at 10 °C. The transport losses as well as the activation losses increase with increasing temperature, but temperature has the least effect on them. Therefore, from the results in Figure 9, it can be concluded that the optimum temperature of the stack is in the range of 40–60 °C. It can be seen that at a temperature of 40 °C, the stack has greatest power output at lower currents, but at higher currents, the stack performs better at 60 °C due to lower ohmic resistance. In the literature, it is generally assumed that the optimal operating temperature range for fuel cells is 60–85 °C. In this case, it is found that while there is a gain in performance at lower current densities and lower temperatures, the instability of the fuel cell increases at higher

current densities. The highest stability over the entire operating range is in the 60–80 °C range, which is consistent with the literature.

Figure 10 shows system efficiency and fuel cell membrane water mass. The plot of efficiency in Figure 10a only confirms the previous conclusions, but it is quite important to emphasize again the difference in efficiency in the low current range, where lower temperatures give much better results (8% difference between 80 °C and 40 °C at 20 A current). The water mass of the membrane is an important parameter, since the protonic conductivity of a polymer membrane strongly depends on the membrane structure and its water content. In Figure 10b, we see the influence of temperature on the total water mass in the membrane, showing that the water mass correlates with the other operating parameters.

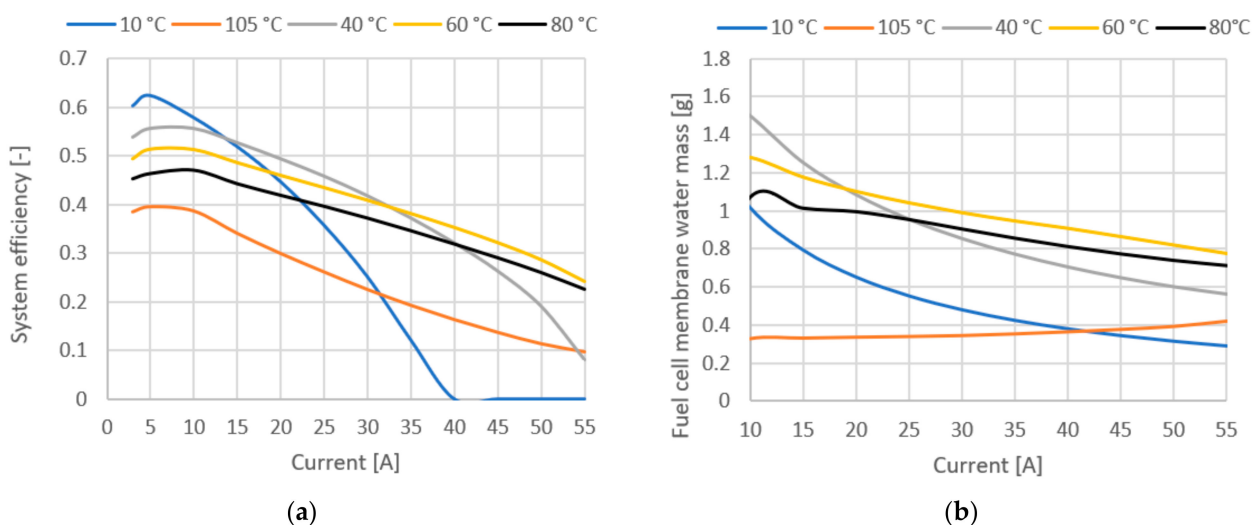


**Figure 10.** (a) System efficiency at various temperatures. (b) Fuel cell membrane water mass.

#### 4. Conclusions

Over the past few years, many numerical studies have been completed to simulate the PEM fuel cell; however, modeling the entire system with the novel reduced dimensionality electrochemical fuel cell model explained in Section 2.2.1. has not yet been adequately explored. In this research, the model of the PEM FC system was developed, calibrated, and the auxiliary compressor and humidifier were sized. Design of experiments was performed to find the optimal stack temperature range. The results showed that the simulation was performed in good agreement with the existing data used in the literature. The model is able to successfully extrapolate the profile of key parameters, such as temperature, pressure, power, voltage, etc. Based on this study, the following conclusions can be drawn:

- The cell performance is only slightly changed with the variations in the stoichiometric ratio of the cathode side. The only difference can be seen on high currents (above 45 A).
- Increasing the cell temperature results in increased fuel cell performance at medium to high currents. The optimal working range is determined by the design of experiments and is in the range of 40–60 °C. In future work, a more complex heat and water management system will be applied to the model to see how this auxiliary system affects the efficiency of the overall system.
- In the low current region, due to lower activation losses, low temperature stacks are significantly more efficient (8% difference between 80 °C and 40 °C at 20 A current).
- Compressor addition is justified only in the high current regions where compressor parasitic losses are outweighed by performance gains (22% power gain at maximal load).

This work shows the level complexity of the PEM FC system model that can still be simulated in real time, and in future research this model is planned to be used as part of software-in-the-loop testing environment. Since most of the work at our department of mechanical engineering is currently focused on marine technologies, the next step in

this research is adding a methanol reformer component to the base model. For marine application, methanol is considered the fuel of the future for large cargo ships due to the safety of storage compared to other alternative fuels. This field has not yet been researched properly, especially in system analysis. In addition to the reformer, the entire system must also be scaled to the level of the ship, which involves complex heat and water management models. This goal is certainly challenging, but the industry's transition to alternative fuels is imminent, and finding a proper solution for zero emission technology is a must.

**Author Contributions:** Conceptualization, T.V., I.T. and G.R.; methodology, T.V. and I.T.; software, T.V.; validation, T.V., I.T. and N.B.Ć.; formal analysis, T.V., I.T., G.R. and N.B.Ć.; writing—original draft preparation, T.V., I.T. and G.R.; writing—review and editing, T.V. and I.T.; funding acquisition, I.T. and G.R. All authors have read and agreed to the published version of the manuscript.

**Funding:** T. Vidović, I. Tolj and G. Radica acknowledges the financial incentive from the Croatian Science Foundation under the project IP.2020-02-6249. I. Tolj and G. Radica acknowledge financial support from EU Horizon 2020/RISE project “Hydrogen fueled utility vehicles and their support systems utilizing metal hydrides HYDRIDE4MOBILITY” (project number: 778307).

**Conflicts of Interest:** The authors declare no conflict of interest.

## References

- Hanif, I.; Raza, S.M.F.; Gago-de-Santos, P.; Abbas, Q. Fossil fuels, foreign direct investment, and economic growth have triggered CO<sub>2</sub> emissions in emerging Asian economies: Some empirical evidence. *Energy* **2019**, *171*, 493–501. [[CrossRef](#)]
- Tetty, U.Y.A.; Gustavsson, L. Energy savings and overheating risk of deep energy renovation of a multi-storey residential building in a cold climate under climate change. *Energy* **2020**, *202*, 117578. [[CrossRef](#)]
- Dudley, B. BP statistical review of world energy. *BP Stat. Rev.* **2018**, *6*, 00116.
- Stolarski, M.J.; Warmański, K.; Krzyżaniak, M.; Olba-Zięty, E.; Stachowicz, P. Energy consumption and heating costs for a detached house over a 12-year period—Renewable fuels versus fossil fuels. *Energy* **2020**, *204*, 117952. [[CrossRef](#)]
- Jouhara, H.; Olabi, A.G. Industrial waste heat recovery. *Energy* **2018**, *160*, 1–2. [[CrossRef](#)]
- Reitz, R.D. Grand challenges in engine and automotive engineering. *Front. Media SA* **2015**, *1*, 1. [[CrossRef](#)]
- Wilberforce, T.; Baroutaji, A.; Soudan, B.; Al-Alami, A.H.; Olabi, A.G. Outlook of carbon capture technology and challenges. *Sci. Total Environ.* **2019**, *657*, 56–72. [[CrossRef](#)]
- Strielkowski, W.; Lisin, E.; Gryshova, I. Climate policy of the European Union: What to expect from the Paris Agreement. *Rom. J. Eur. Aff.* **2016**, *16*, 68.
- Böhringer, C. The Kyoto protocol: A review and perspectives. *Oxf. Rev. Econ. Policy* **2003**, *19*, 451–466. [[CrossRef](#)]
- Ma, F.; Wang, Y.; Liu, H.; Li, Y.; Wang, J.; Ding, S. Effects of hydrogen addition on cycle-by-cycle variations in a lean burn natural gas spark-ignition engine. *Int. J. Hydrogen Energy* **2008**, *33*, 823–831. [[CrossRef](#)]
- White, C.; Steeper, R.; Lutz, A. The hydrogen-fueled internal combustion engine: A technical review. *Int. J. Hydrogen Energy* **2006**, *31*, 1292–1305. [[CrossRef](#)]
- Thomas, C. Fuel cell and battery electric vehicles compared. *Int. J. Hydrogen Energy* **2009**, *34*, 6005–6020. [[CrossRef](#)]
- Alaswad, A.; Palumbo, A.; Dassisi, M.; Olabi, A.G. Fuel Cell Technologies, Applications, and State of the Art. A Reference Guide. In *Reference Module in Materials Science and Materials Engineering*; Elsevier: Amsterdam, The Netherlands, 2016. [[CrossRef](#)]
- Wilberforce, T.; Olabi, A.G. Performance prediction of proton exchange membrane fuel cells (PEMFC) using adaptive neuro inference system (ANFIS). *Sustainability* **2020**, *12*, 4952. [[CrossRef](#)]
- Wilberforce, T.; Olabi, A.G. Design of experiment (DOE) analysis of 5-cell stack fuel cell using three bipolar plate geometry designs. *Sustainability* **2020**, *12*, 4488. [[CrossRef](#)]
- Sorlei, I.-S.; Bizon, N.; Thounthong, P.; Varlam, M.; Carcadea, E.; Culcer, M.; Iliescu, M.; Raceanu, M. Fuel cell electric vehicles—A brief review of current topologies and energy management strategies. *Energies* **2021**, *14*, 252. [[CrossRef](#)]
- Wang, Y.; Yuan, H.; Martinez, A.; Hong, P.; Xu, H.; Bockmiller, F.R. Polymer electrolyte membrane fuel cell and hydrogen station networks for automobiles: Status, technology, and perspectives. *Adv. Appl. Energy* **2021**, *2*, 100011. [[CrossRef](#)]
- Palencia, J.C.G.; Nguyen, V.T.; Araki, M.; Shiga, S. The role of powertrain electrification in achieving deep decarbonization in road freight transport. *Energies* **2020**, *13*, 2459. [[CrossRef](#)]
- Piraino, F.; Genovese, M.; Fragiaco, P. Towards a new mobility concept for regional trains and hydrogen infrastructure. *Energy Convers. Manag.* **2021**, *228*, 113650. [[CrossRef](#)]
- de Lorenzo, G.; Andaloro, L.; Sergi, F.; Napoli, G.; Ferraro, M.; Antonucci, V. Numerical simulation model for the preliminary design of hybrid electric city bus power train with polymer electrolyte fuel cell. *Int. J. Hydrogen Energy* **2014**, *39*, 12934–12947. [[CrossRef](#)]
- Shih, N.-C.; Weng, B.-J.; Lee, J.-Y.; Hsiao, Y.-C. Development of a 20 kW generic hybrid fuel cell power system for small ships and underwater vehicles. *Int. J. Hydrogen Energy* **2014**, *39*, 13894–13901. [[CrossRef](#)]

22. Pourrahmani, H.; Bernier, C.M.I.; van Herle, J. The application of fuel-cell and battery technologies in unmanned aerial vehicles (UAVs): A dynamic study. *Batteries* **2022**, *8*, 73. [[CrossRef](#)]
23. Yue, M.; al Masry, Z.; Jemei, S.; Zerhouni, N. An online prognostics-based health management strategy for fuel cell hybrid electric vehicles. *Int. J. Hydrogen Energy* **2021**, *46*, 13206–13218. [[CrossRef](#)]
24. Vichard, L.; Steiner, N.Y.; Zerhouni, N.; Hissel, D. Hybrid fuel cell system degradation modeling methods: A comprehensive review. *J. Power Sources* **2021**, *506*, 230071. [[CrossRef](#)]
25. Luciani, S.; Tonoli, A. Control Strategy Assessment for Improving PEM Fuel Cell System Efficiency in Fuel Cell Hybrid Vehicles. *Energies* **2022**, *15*, 2004. [[CrossRef](#)]
26. Crespi, E.; Guandalini, G.; Gößling, S.; Campanari, S. Modelling and optimization of a flexible hydrogen-fueled pressurized PEMFC power plant for grid balancing purposes. *Int. J. Hydrogen Energy* **2021**, *46*, 13190–13205. [[CrossRef](#)]
27. Staffell, I.; Scamman, D.; Abad, A.V.; Balcombe, P.; Dodds, P.E.; Ekins, P.; Shah, N.; Ward, K.R. The role of hydrogen and fuel cells in the global energy system. *Energy Environ. Sci.* **2019**, *12*, 463–491. [[CrossRef](#)]
28. Kravos, A.; Ritzberger, D.; Tavčar, G.; Hametner, C.; Jakubek, S.; Katrašnik, T. Thermodynamically consistent reduced dimensionality electrochemical model for proton exchange membrane fuel cell performance modelling and control. *J. Power Sources* **2020**, *454*, 227930. [[CrossRef](#)]
29. Springer, T.E.; Wilson, M.S.; Gottesfeld, S. Modeling and experimental diagnostics in polymer electrolyte fuel cells. *J. Electrochem. Soc.* **1993**, *140*, 3513. [[CrossRef](#)]
30. AVL Cruise-M User Manual. Available online: <https://www.avl.com/cruise-m> (accessed on 29 September 2022).
31. Wang, X.; Qu, Z.; Lai, T.; Ren, G.; Wang, W. Enhancing water transport performance of gas diffusion layers through coupling manipulation of pore structure and hydrophobicity. *J. Power Sources* **2022**, *525*, 231121. [[CrossRef](#)]
32. Dubose, R. Enthalpy Wheel Humidifiers. In Proceedings of the 2002 Fuel Cell Seminar, Palm Springs Convention Center, Palm Springs, CA, USA, 18–21 November 2002.
33. Chen, D.; Peng, H. A thermodynamic model of membrane humidifiers for PEM fuel cell humidification control. *J. Dyn. Sys. Meas. Control* **2005**, *127*, 424–432. [[CrossRef](#)]
34. Polak, A.; Grzeczka, G.; Piłat, T. Influence of cathode stoichiometry on operation of PEM fuel cells' stack supplied with pure oxygen. *J. Mar. Eng. Technol.* **2017**, *16*, 283–290. [[CrossRef](#)]